P1.8 A LIDAR-RADAR OBSERVING SYSTEM FOR MONITORING OPTICAL AND MICROPHYSICAL PROPERTIES OF CIRRUS

Cristian Mitrescu[1,2*] John Haynes[3] Steve Miller[2]

[1]American Society for Engineering Education.
[2]Naval Research Laboratory, Marine Meteorology Division, Monterey, California.
[3]Department of Atmospheric Science, Colorado State University, Fort Collins, Colorado.

1. INTRODUCTION

Understanding the climate of Earth and the way climate varies in time requires a quantitative understanding of the way water cycles back and forth between its main reservoirs in the atmosphere and at the Earth's surface. Processes relating to the atmospheric branch of the hydrological cycle play an especially critical role in climate change especially through cloud and water vapor feedbacks (Held and Soden, 2000). Understanding and ultimately quantifying cloud feedbacks remains a significant challenge to climate research.

Since cirrus clouds are ubiquitous (Liou, 1986) and their bulk microphysical properties highly variable (Heymsfield, 1972) and difficult to measure *in situ*, satellite-based remote sensing methods loom as important for studying the influence of cirrus on the global climate system. The verification of these methods is thus of critical importance.

This work presents an analysis procedure of aircraft remote sensing data that attempts to define the properties of cirrus clouds that eventually could be used to address some of the questions posed above. Thus, a method of retrieval of cloud microphysical parameters that uses vertical profiles of both radar reflectivity and lidar backscatter is introduced. The retrieval problem is formulated in terms of an optimal estimation framework (Jazwinski, 1970) as introduced by Stephens et al. (2001). Present work expands upon optimal estimation technique by introducing a modification that serves to increase computational efficiency for systems represented by large retrieval vectors and hastens convergence to a solution. The lidar-radar retrieval algorithm is applied to data collected during the CRYSTAL-FACE campaign that occurred in south Florida during July 2002. Retrieved optical and microphysical parameters are compared against *in-situ* measurements, validating the method.

2. A NOVEL IMPLEMENTATION OF OPTIMAL ESTIMATION

The problem of determining the state of a system from noisy measurements is called *estimation*, or *filtering*. A key aspect in solving these problems is the specification of a physical model that relates the measurements to the state variables which is referred to as the *forward model* or the *mapping operator*. The most probable event described by such a model is the one that minimizes the cost function, which under the assumption of Gaussian statistics (Jazwinski, 1970) can be written as:

$$J(\boldsymbol{x}) = \frac{1}{2} \sum_{s,q} [y^s - H^s(\boldsymbol{x}, \boldsymbol{b})] \; \boldsymbol{R}_{s,q}^{-1} \; [y^q - H^q(\boldsymbol{x}, \boldsymbol{b})] \quad , \quad (1)$$

where we ignore the *a priori* term (a reasonable assumption for the present application). Here $s, q = 1, ..., L$ denotes the measurement or constraint used at a particular location, H is the (nonlinear) forward model describing such a measurement or constraint, $\boldsymbol{b}$ is the forward model vector of parameters, and $\boldsymbol{R}$ is the error covariance matrix associated with the measurements and/or constraints. The forward model vector of parameters is a list of physical variables needed in the description of the forward model. They are being held constant, although some of them may display some variability/uncertainty within the measurements. We define one component of the state vector by x_m, where m identifies the physical variable. The dimension of the state vector is then the sum of all its variables (chose here to match the numbers of measurements and/or constraints L). Like in the method mentioned above, the solution to our problem is given by:

$$\boldsymbol{A}_{mk} \; \delta x_k = \boldsymbol{G}_m \quad , \quad m, k = \overline{1, M} \quad , \quad (2)$$

with

$$\boldsymbol{A}_{mk} = \sum_{sq} \frac{\partial H^s}{\partial x_m} \; \boldsymbol{R}_{s,q}^{-1} \; \frac{\partial H^q}{\partial x_k} \quad (3)$$

and

$$\boldsymbol{G}_m = \sum_{sq} \frac{\partial H^s}{\partial x_m} \; \boldsymbol{R}_{s,q}^{-1} \; [y^s - H^s(\boldsymbol{x}_0)] \quad , \quad (4)$$

where M is the dimension of the subset of components of state vector, and $\boldsymbol{x}_0$ is the state vector determined at a previous iteration step. In order to complete the minimization process, the above procedure must be applied to the following subset of components of state vector until all components are adjusted. The advantage of the formulation expressed by (2), (3), and (4) when $M < L$ over the more common approach that sets $M = L$, lies in its reduced dimension. The choice for the number of elements M and the order of the state vector components depends a lot on the forward model H and the dimension of the state vector.

*Corresponding author address: Cristian Mitrescu, Naval Research Laboratory, 7 Grace Hopper Ave. MS#2, Monterey, CA 93943-5502; e-mail: mitrescu@nrlmry.navy.mil.

An important aspect of the optimal estimation method resides in the computation of error covariance matrix of the state vector, defined as follows:

$$\boldsymbol{S}^{-1}_{m,k} = \sum_{s,q} \frac{\partial H^s}{\partial x_m}\, \boldsymbol{R}^{-1}_{s,q}\, \frac{\partial H^q}{\partial x_k} \quad , \quad m,k = \overline{1,L} \quad , \qquad (5)$$

which is just the inverse of an $\boldsymbol{A}$ matrix at full dimension, since we neglected the *a priori* error covariance matrix from our cost function evaluation. We thus avoid any unwanted dependence of our solution to the *a priori* information. The diagonal elements of $\boldsymbol{S}$ are variances of the state vector and give a measure of the uncertainty in the retrieval; off-diagonal elements are just cross-correlations of their errors. For the purpose of estimating the above errors, the observation error covariance matrix $\boldsymbol{R}$ contains both measurement errors as well as errors due to uncertainty in model parameters $\boldsymbol{b}$:

$$\boldsymbol{R}_{s,q} = \boldsymbol{Y}_{s,q} + \sum_{i,j} \frac{\partial H^s}{\partial b_i}\, \boldsymbol{B}_{i,j}\, \frac{\partial H^q}{\partial b_j} \quad . \qquad (6)$$

Here $\boldsymbol{B}$ is the model parameter error covariance matrix and $\boldsymbol{Y}$ is the measurement error covariance matrix.

3. APPLICATION TO THE LIDAR-RADAR MODEL

This section describes how the general method presented above is applied to lidar and radar measurements to infer cloud optical and microphysical parameters. The first stage in the application is to set the basis for the forward model. This means to define analytical relationships between the state vector (i.e. physical variables) and measured vector (i.e. measured quantities).

3.1 Microphysical model

In-situ microphysical observations of cirrus clouds reveal that ice particles display a wide variety of complex shapes and dimensions with a strong dependence on dynamical and thermodynamical factors (Heymsfield et al., 2002). Despite this increased complexity, for radiative purposes, we can rely on averaged particle properties which were shown to be more suitable for an analytical description. Following previous studies (Verlinde et al., 1990), we assume a fixed Gamma size distribution for the cloud ice particles:

$$n(D) = N_0\, \frac{1}{\Gamma(\nu)} \left(\frac{D}{D_0}\right)^{\nu-1} \frac{1}{D_0}\, \exp\left(-\frac{D}{D_0}\right) \quad , \qquad (7)$$

where the width parameter ν is a constant, and diameter D represents the maximum dimension of a particle as measured by an imaging probe. N_0 is total number particle concentration, while D_0 is characteristic diameter. Since ice crystals display complex shape, for the purpose of defining an analytical forward model, we used empirical relationships relating projected area, volume, and mass of ice cloud particles to the maximum dimension. Empirical fits from measured data, provided throughout the literature (e.g. Brown and Francis, 1995; Mitchell et al., 1996; etc.), represent these relationships as power laws of the form:

$$X(D) = g_X\ D^{f_X} \quad , \qquad (8)$$

where X is the variable of interest (area, volume, mass, density, etc.) and g_X and f_X are cloud averaged fit coefficients. However, the fit coefficients show a large range of variation over the multitude of observed cirrus clouds (Heymsfield et al., 2004a, b).

3.2 Lidar model

For the lidar system, the attenuated backscatter can be expressed as (Mitrescu et al., 2004):

$$\beta'(i) = \frac{C(i)}{2\ S\ \delta z} \left[1 - e^{-2\ \beta_{ext}(i)\ \delta z}\right] \cdot e^{-2\cdot\tau(i)} \quad , \qquad (9)$$

where S is lidar ratio (in sr), C describes multiple scattering (MS) contribution, β_{ext} is extinction coefficient, and δz is lidar's vertical resolution. $\tau(i)$ is the cloud optical depth up to level i, increasing with lidar penetration depth:

$$\tau(i) = \left[\sum_{k=1}^{i-1} \beta_{ext}(k)\right] \cdot \delta z \quad . \qquad (10)$$

The lidar ratio S, considered constant throughout the cloud layer, is determined according to the technique described in McGill et al. (2003). MS effects are initially estimated following Mitrescu (2004), then, as the iterative process (2) converges toward the solution, we choose the formulation of Eloranta (1998):

$$C(i) = \sum_{m=1}^{4} \frac{P_m(i)}{P_1(i)} \quad , \qquad (11)$$

where P_m represents the contribution to the backscatter signal from the m-th order of scatter. This approach clearly speeds up the convergence process, without losing accuracy when evaluating the C term.

When only lidar attenuated backscatter and lidar ratio are available - as expressed by (9 - 11), the state vector is reduced in both dimension and information content. However, key cloud optical properties, such as the profile of the extinction coefficient, can still be inferred from such measurements. We can thus define the measurement vector and the state vector associated with what we can call a β model (that only uses information from the lidar system) in the form:

$$\boldsymbol{y} = [\ln\beta'(1), ..., \ln\beta'(n)] \qquad (12)$$

$$\boldsymbol{x} = [\beta_{ext}(1), ..., \beta_{ext}(n)] \quad . \qquad (13)$$

We point out that β model requires no specification of the particle size distribution (with the exception of MS effects), just the value of the extinction coefficient β_{ext}.

In order to conclude our lidar model, we note that at the non absorbing lidar wavelengths, the extinction efficiency - which equals the scattering efficiency, approaches the value of two. Thus, the extinction coefficient can be expressed as:

$$\beta_{ext}(i) = 2\ g_A\ \frac{\Gamma(\nu + f_A)}{\Gamma(\nu)}\ N_0(i)\ D_0^{f_A}(i) \quad , \qquad (14)$$

where g_A and f_A are fitting coefficients describing cross sectional area as function of diameter for non-spherical ice particles. We note that it is at this point that non-spherical effects are revealed, underlying the idea that these effects are defined and characterized at microphysical level. Cloud optical properties (extinction coefficient, optical depth, lidar ratio), as determined by the lidar system alone, although influenced by it, cannot reveal such a structure in the absence of an explicit formulation. This is clearly explained by the above form of the state vector (13).

3.3 Radar model

For Rayleigh scattering, the backscatter cross section is proportional to the square of the product between the scalar average volume polarizability and the volume (excluding hollow regions) of the scatterer (Donovan and van Lammeren, 2001). Thus, the radar reflectivity can be expressed as:

$$\mathcal{Z}_R(i) = g_Z \, \frac{\Gamma(\nu + f_Z)}{\Gamma(\nu)} \, N_0(i) \, D_0^{f_Z}(i) \quad , \qquad (15)$$

where g_Z and f_Z are fit coefficients describing ice crystals non-spherical effects, and subscript R indicates Rayleigh approximation. Since we seek to retrieve cloud microphysical properties using a lidar-radar system, it is useful to rewrite (15) in terms of (14) as:

$$\mathcal{Z}_R(i) = \frac{g_Z}{2 \, g_A} \, \frac{\Gamma(\nu + f_Z)}{\Gamma(\nu + f_A)} \, \beta_{ext}(i) \, D_0^{f_Z - f_A}(i) \quad , \qquad (16)$$

which is equivalent to the form proposed by Donovan and van Lammeren (2001) The above definition is usually expressed using dBZ units, as (Heymsfield et al., 2002):

$$Z(i) \; [\text{dBZ}] = 10 \cdot \log \mathcal{Z}_R(i) - 7.2 - M \quad , \qquad (17)$$

where M is a correction factor due to Mie effects (Bohren and Huffman, 1983; Mitrescu et al., 2004).

From (15-17) we note that contrary to the lidar model, the formulation of the radar model requires knowledge about the microphysical structure. Therefore, this structure (namely N_0 and D_0) cannot be retrieved at each level using this formulation. However, by adding information from the lidar system, such a task is possible.

3.4 Forward model: $Z - \beta$ algorithm

When measurements from both instruments are available, based on (9-11, 14) and (15-17), we define a $Z - \beta$ model for describing the lidar-radar system. We can thus define the measurement vector and the state vector for this system as:

$$\boldsymbol{y} = [\ln \beta'(1)), ..., \ln \beta'(n), Z(1), ..., Z(n)] \qquad (18)$$

$$\boldsymbol{x} = [\beta_{ext}(1), ..., \beta_{ext}(n), D_0(1), ..., D_0(n)] \quad , \qquad (19)$$

where lidar and radar layers are identified by their indexes. When radar signal is below the minimum detectable level, we simply ignore the radar information and set the characteristic diameter to a pre-specified value (i.e. D_0 =10 μm). Here we consider all n lidar layers, some of which are overlapped by radar. Solving for the above form of the state vector follows the steps described in previous section.

For the overlap region, once profiles of N_0 and D_0 are retrieved, profiles of ice water content (IWC) are obtained by simply integrating the individual mass particle over the size distribution:

$$IWC(i) = g_m \, \frac{\Gamma(\nu + f_m)}{\Gamma(\nu)} \, N_0(i) \, D_0^{f_m}(i) \quad . \qquad (20)$$

As before, this expression accounts for non-spherical effects. From the above equation, we can also estimate the ice water path (IWP) for the overlap region, as:

$$IWP = \sum_{i=1}^{n_2} IWC(i) \, \delta z \quad . \qquad (21)$$

We thus conclude our lidar-radar forward model formulation and the definition of derived quantities that characterize both optical and microphysical properties of ice cirrus cloud, with a full description of ice particle non-spherical effects.

3.5 Initial guess

The iterative process to obtain solution required by the optimal estimation technique is sensitive to the initial guess of the state vector. In order to speed up the iterative process, the initial guess must be as close to the solution as possible. For this we can employ various techniques. A common procedure is to simplify the system of equations to a level that permits analytic solutions, later used as initial guess $\boldsymbol{x}_0$.

The lidar model yields:

$$\beta^{\star}_{ext}(i) = -\frac{1}{2 \, \delta z} \cdot \ln \left[1 - \frac{2 \, S \, \delta z \, \beta'(i) \, e^{2 \, \tau(i)}}{C(i)} \right] \quad . \qquad (22)$$

Although in an analytical form, the above equation is subject to the *a priori* knowledge of MS effects; therefore, the aforementioned MS parameterization is useful.

When adding radar information to the lidar system, an analytical solution is again possible. From (14), (16), and (22) we can estimate characteristic diameter:

$$D_0^{\star}(i) = \left\{ \frac{2 \, g_A}{g_Z} \, \frac{\Gamma(\nu + f_A)}{\Gamma(\nu + f_Z)} \, \frac{10^{[Z_M(i)]/10}}{\beta^{\star}_{ext}(i)} \right\}^{1/(f_Z - f_A)} \qquad (23)$$

and particle number concentration:

$$N_0^{\star}(i) = \frac{1}{2 \, g_A} \, \frac{\Gamma(\nu)}{\Gamma(\nu + f_A)} \, \beta^{\star}_{ext}(i) \, [D^{\star}(i)]^{-f_A} \quad . \qquad (24)$$

We note that the above expressions (22 - 24), although not the exact solutions to our observing system, eliminate the need for an *a priori* solution and all the complicated algebra that follows. Also clear from the above approximation is that the components of the state vector as determined from the above analytical solution, are obtained somewhat iteratively. In the following section, we apply the proposed retrieval algorithm on real data.

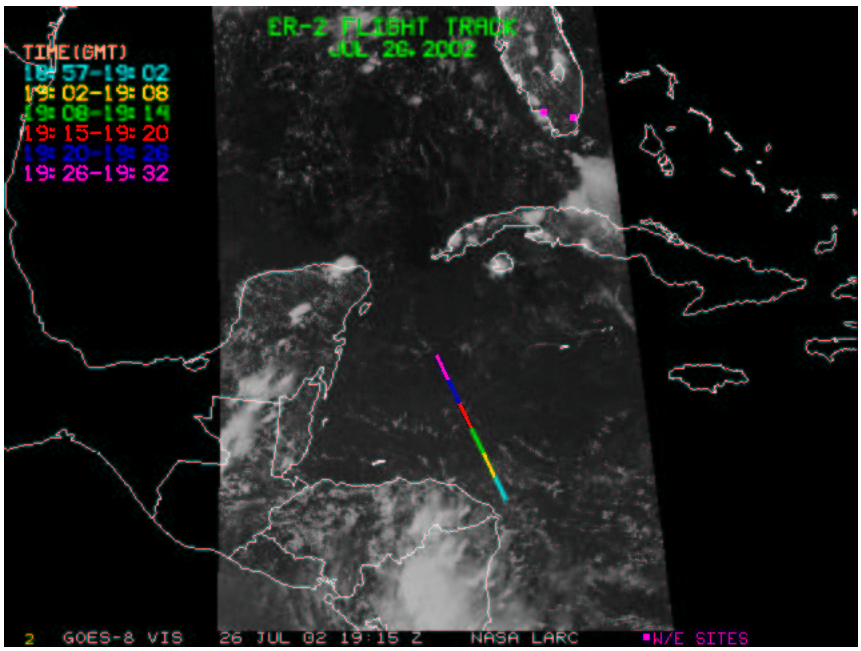

Figure 1: GOES-8 visible spectra image. ER-2 flight track is superimposed.

4. APPLICATION TO CRYSTAL-FACE DATA

The Cirrus Regional Study of Tropical Anvils and Cirrus Layers - Florida Area Cirrus Experiment (CRYSTAL-FACE) campaign took place in southern Florida in the summer of 2002. During this campaign, measurements of convection, anvils and other tropical cirrus clouds were obtained with a combination of active and passive sensors aboard six research aircraft based in Key West and at two ground sites in southern Florida.

4.1 26 July case study description

On 26 July 2002, the ER-2 high altitude research aircraft flew a flight track from Key West to just off the coast of Nicaragua. This case study is concerned with the return flight leg toward the north-northwest, when the ER-2 flew over a cirrus shield located off the Nicaraguan coast. This cirrus was also being sampled *in situ* by the lower flying WB-57 aircraft. Figure 1 shows the flight track superimposed on the visible GOES-8 satellite image.

The cirrus shield that was sampled between approximately 18:10 and 19:10 UTC was associated with active convection over Nicaragua. This case study focuses on a six minutes window of observations that were collected late in the period, during which time the cloud layer was approximately 3.5 km thick.

4.2 Lidar-Radar observing system

Cloud data from two active instruments aboard the ER-2 high altitude research aircraft were used in this study. Lidar data were obtained from the Cloud Physics Lidar (CPL) that also flew aboard the ER-2 during CRYSTAL-FACE (http://cpl.gsfc.nasa.gov/). The CPL is a pulsed lidar system that simultaneously transmits at 355, 532, and 1064 nm; only the 532 nm visible channel was used in this study. The radar data are those obtained from the 94 GHZ Cloud Radar System (CRS, Li et al., 2004), a W-band Doppler radar with a peak transmitting power of 1.7 kW and a minimum detectable signal of approximately -35 dBZ at 15 km altitude and -20 dBZ at the surface. For processing by the algorithm, the attenuated backscatter from the lidar was matched, both spatially and temporally, to the radar reflectivity. Nadir radar reflectivity, and lidar attenuated backscatter for the case study are shown in Figure 2.

4.3 In-situ measurements of cirrus

Ice water content data for the flight were obtained by the Harvard Total Water Instrument (TWI) onboard the WB-57 aircraft (Weinstock et al., 1994). Ice water volume mixing ratio data were converted to IWC using measured pressure and temperature for comparison with the retrieval.

In situ observations of the size spectra were provided by the SPP-100 scattering spectrometer (SPP), also mounted on the WB-57. The SPP data was used to calculate the number concentration and characteristic diameter of an equivalent Gamma particle size distribution with $\nu = 2$ (as it is assumed by the lidar-radar model):

$$D_0^{(SPP)} = \frac{1}{4} \cdot \frac{< D^3 >}{< D^2 >} \quad , \tag{25}$$

where the means are calculated from the measured particle size distributions. Figure 3 shows such a particular

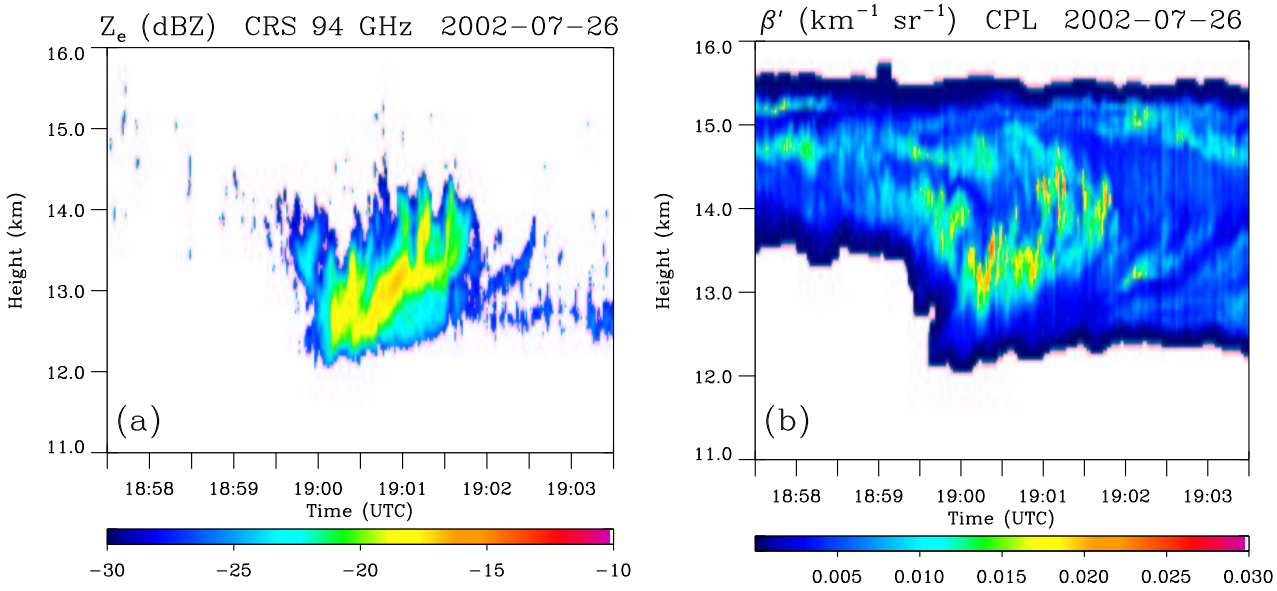

Figure 2: 26 July 2002: (a) CRS 94 GHz Radar data, (b) CPL 532 nm Lidar data.

case: solid line - as measured by SPP, and dots - as determined by (25). With dash line is the retrieved Gamma particle size distribution, that closely matches the measured distribution of larger particles. We refer here to particles with characteristic diameter around and larger than 15 μm, that contribute more to the radar signal than smaller particles. It also explains the longer tail of the retrieved Gamma distribution.

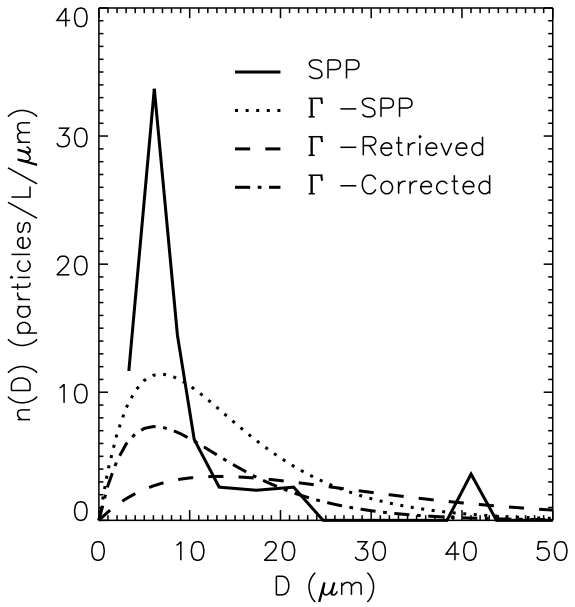

Figure 3: Particle size distribution: solid - from SPP probe; dots - equivalent Gamma distribution; dash - retrieved Gamma distribution; dot-dash - same as above, with correction for small particles.

However, since the SPP probe indicates smaller ice crystals, we can determine an equivalent Gamma particle size distribution valid for solid ice spheres (i.e. smaller ice crystals). By simply using (15) with fit parameters adjusted for solid ice spheres, we deduce that the characteristic diameter of such an equivalent distribution of solid ice spheres is related to the one assuming non-spherical effects as:

$$D_0^{(s)} = 0.67\, D_0^{0.87} \quad . \tag{26}$$

The Gamma particle size distribution of the equivalent solid ice spheres is represented with dotted-dash line. This new form of distribution is closer to the one deduced from the measurements, and correctly accounts for density effects applied in the description of the lidar-radar observing system.

The conclusion of this exercise is that small particles are yet to be correctly retrieved by the lidar-radar system. This is due to both bimodal and density effects that cannot be captured by the definition of a single Gamma particle size distribution, nor by the assignment of some fixed values for the fit parameters. More retrieval results are presented in the following subsection.

4.4 Retrieval results

In areas where radar was not sensitive enough to observe thin cirrus, lidar observations alone was used to retrieve the vertical profile of extinction coefficient. Profile of the extinction coefficient for the case study considered here is presented in Figure 4(a). The mean extinction coefficient is around 0.3 km^{-1}, with values up to around 2 km^{-1} in the overlap areas.

By adding radar information to the lidar observing system, we are able to infer vertical profiles of D_0, N_0, and IWC via the $Z - \beta$ algorithm described above, shown in

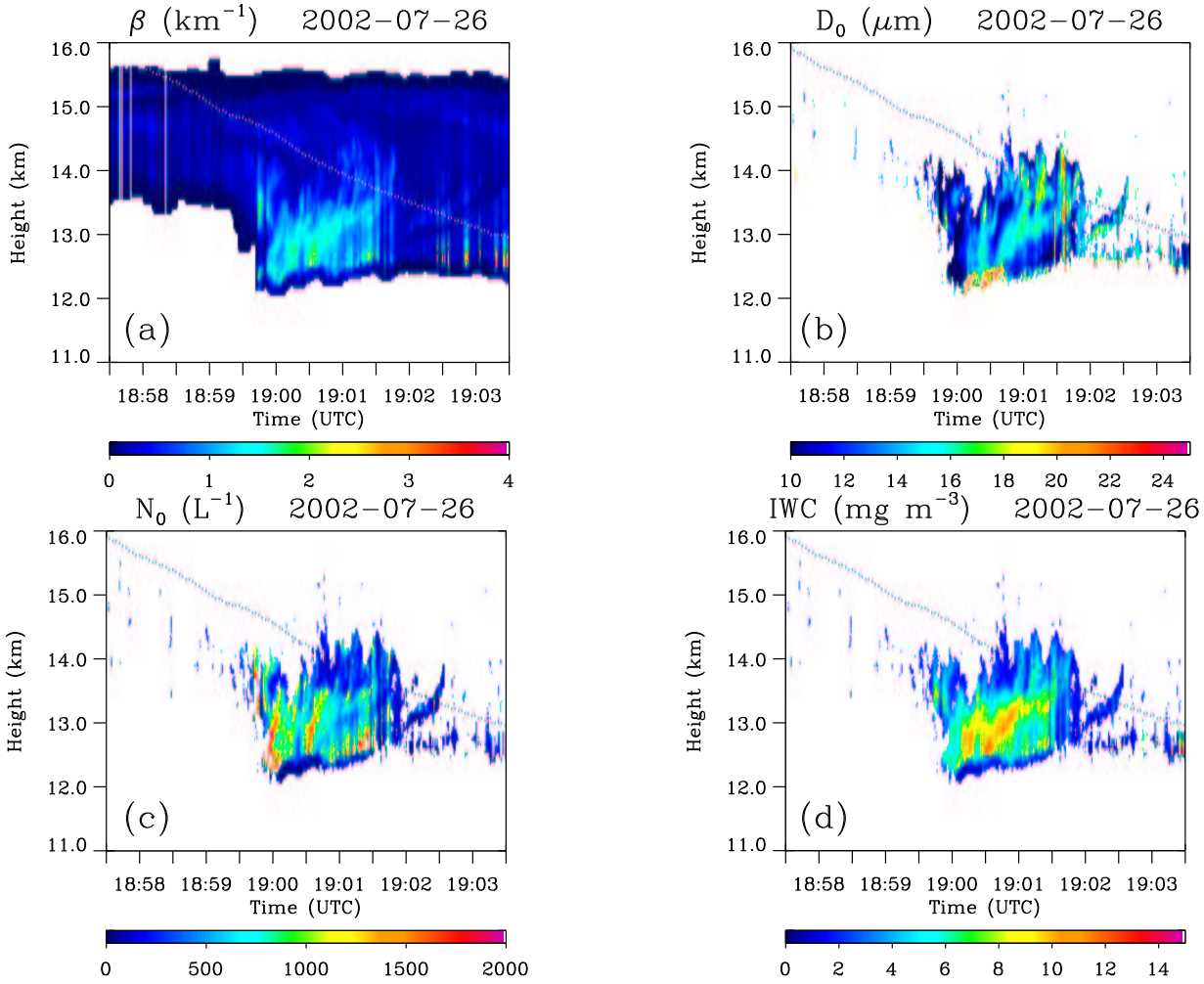

Figure 4: Time-height plots of retrieved (a) Extinction coefficient β_{ext}, (b) Characteristic diameter D_0, (c) Particle number concentration N_0, and (d) IWC. Superimposed is the WB-57 flight track.

Figure 4(b), (c), and (d). For the overlap regions, the retrieved values of D_0 ranges between 0.005 and 0.1 mm, indication of relatively small ice crystals. The mean value is centered at about 11 μm, which yields an effective ice crystal radius of about 22 μm. The particle number concentration N_0 shows a large domain of variation with retrieved values of up to 10^4 particle per liter. While smaller values are naturally detected at cloud boundaries, there are regions in cloud displaying large vertical variations of this parameter, underlying once more the importance of vertical profiling of clouds. Finally, the computed IWC varies between 0.1 and 10 mg m^{-3}, with a pattern closely related to the radar reflectivity. These correlations will be studied further below. The relative errors as calculated by the optimal estimation method, are shown in Figure 5. From the figure, we see that errors in all fields increase dramatically at the far-end of the cloud, where the lidar signal becomes uncertain, due to the reasons explained before. At these locations, errors can exceed 100 % in all retrieved fields. Of the retrieved variables, N_0 shows the largest errors while D_0 and β_{ext} display only a relatively small degree of uncertainty. In the case of IWC, the dramatic errors increase at the far-end of the cloud, is partly due to the fact that this is a derived quantity, influenced by the large uncertainties in N_0 field. The main source of errors comes from uncertainties of the model parameters, amplified by the two-way transmittion term in the lidar model. Moreover, all these errors may be subject to bias errors, but this is a problem yet to be solved. However, for optically thin regions of the cloud, the errors are within reasonable limits, not exceeding 10 % of the retrieved field. We conclude that overall, the retrievals are satisfactory from this point of view and hope that additional measurements and information about model parameters will further lower the level of these errors.

In the following, we extend the discussion started in the previous subsection by comparing our retrieved variables against the *in-situ* measurements. Figure 6 shows such a comparison over the entire cloud penetration, where symbols represent measurements and lines re-

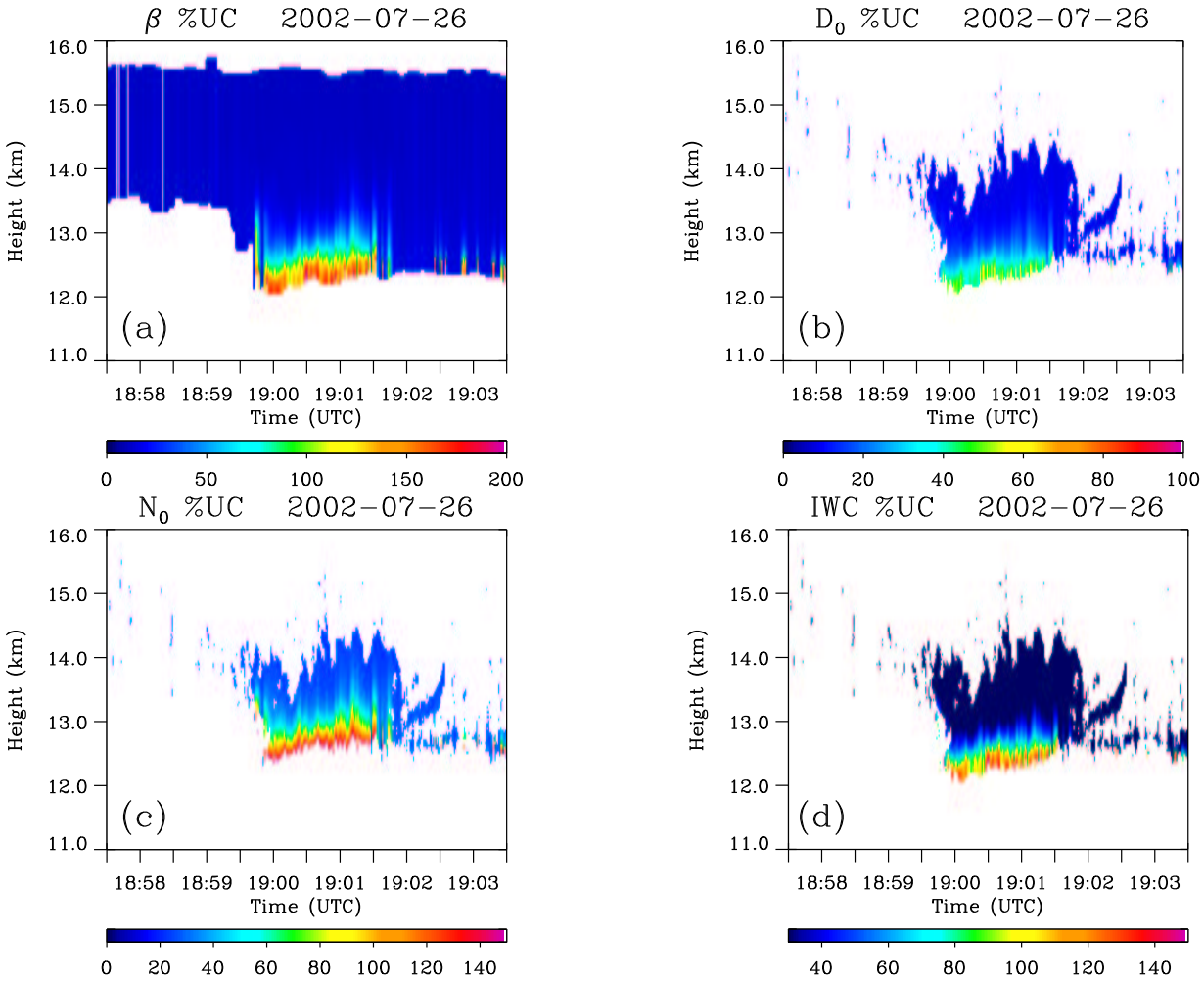

Figure 5: Time-height plots of relative errors of retrieved (a) Extinction coefficient β_{ext}, (b) Characteristic diameter D_0, (c) Particle number concentration N_0, and (d) IWC.

trieved variables. The values of retrieved variables are considered to be coincidental with measurements if they are within one range gate of the reported WB-57 altitude. The IWC, as measured by the TWI instrument, slowly varies between 1 and 4 mg m^{-3}, with the retrieved IWC values in close range, although showing a more dynamic variation from one point to another. A similar behavior is observed for both N_0 and D_0, displayed in panels (b) and respectively (c) of the figure. As mentioned in the previous section, since small ice crystals dominate this top portion of the cloud, they are not properly retrieved by the lidar-radar algorithm, that implicitly assumes larger ice crystals. The corrected $D_0^{(s)}$ values are represented by the thin line and closely match the observed values. Overall, these results demonstrate the validity of our forward lidar-radar model, but also shows its limitations in detecting smaller ice crystals.

For completeness, we also present the calculated values of cloud optical depth (τ) - as seen by lidar, and ice water path (IWP) - valid only for the lidar-radar overlap region (see Figure 7). We note that the cirrus cloud is relatively thin - thus penetrated by lidar, with optical depth ranging from 0.2 to around 1.8. When radar signal is measurable, IWP tops around 10 g m^{-2}, then, as radar signal fades out, it drops to values around 2 g m^{-2}, indication of a very thin cirrus cloud layer.

4.5 Validating empirical relationships

We now shift focus on the possible correlations between various model variables, as a possible way of validating results and/or improving model parameterization.

Of interest is the relationship between the radar reflectivity Z and the ice water content IWC. In literature such a relationship is written as:

$$\lg IWC[\text{mg m}^{-3}] = c \cdot Z[\text{dBZ}] + d \quad , \qquad (27)$$

which is plotted on panel (a) of Figure 8. The retrieval algorithm yields mean values of 0.073 and 2.24 for coefficients c and d respectively. Here we have filter out

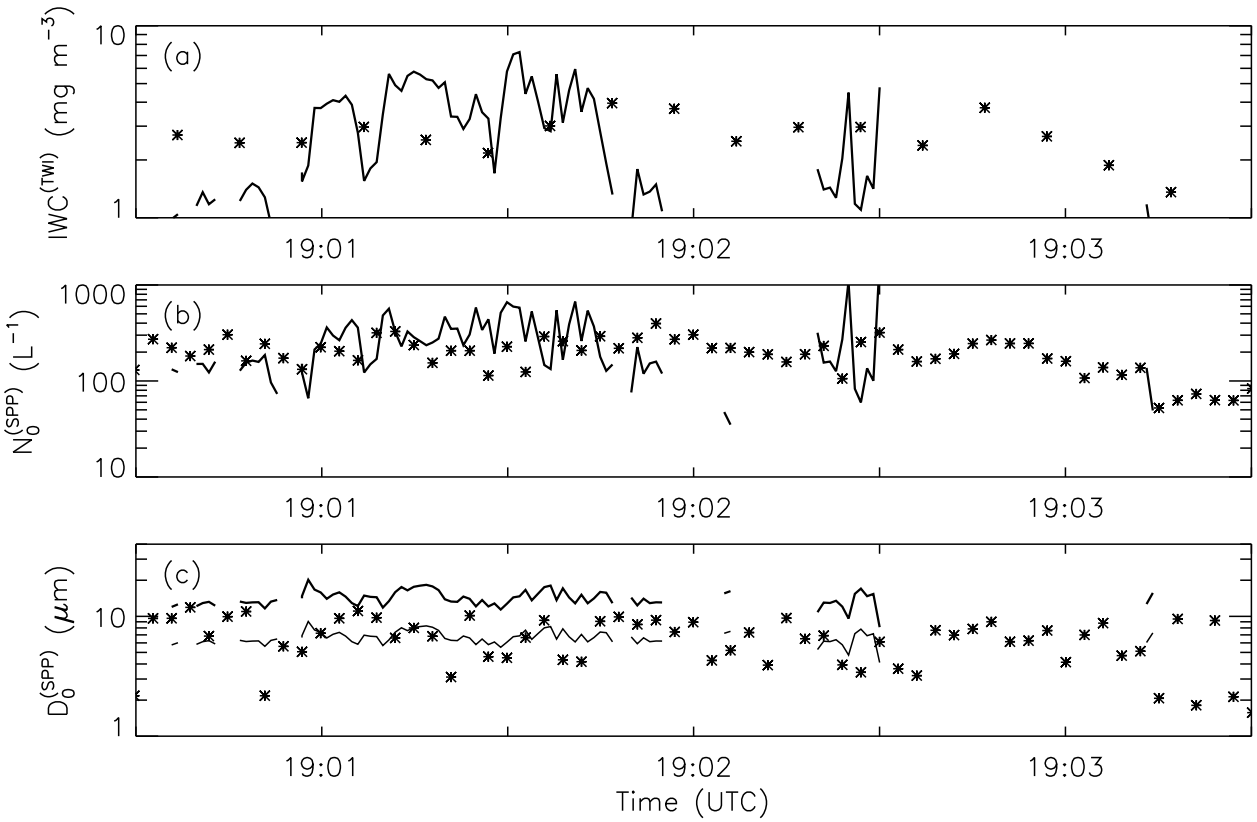

Figure 6: Observed and retrieved values of (a) IWC, (b) total particle number concentration, and (c) particle effective diameter. Solid lines show retrieved values and asterisks show observations. The thin line in (c) represents values of $D_0^{(s)}$ of equivalent solid ice spheres. See text for details.

retrieved values of IWC with errors larger than 30 %, occuring mostly at the far-end of the cloud, for reasons explained before. These fit coefficients are within the previously reported values (e.g. Brown et al., 1995), thus further validating our results.

If (27) is consider valid, then, from (20) and (16), we can speculate that a relationship between N_0 and D_0 is relevant. We must mention that such a relationship was also observed by Heymsfield, (2002). Thus, we write:

$$N_0[\mathrm{L}^{-1}] = 10^B \cdot D_0^A[\mu\mathrm{m}] \quad , \tag{28}$$

where A and B are empirical coefficients to be determined from observations. As with (27), the above equation, if realistic, represents a property valid over several interacting cloud layers. We suggest that exponent A may indicate ice crystals growth regimes. The scatter plot of N_0 and D_0, presented on panel (b) of the figure, shows a strong correlation between these two microphysical parameters, suggesting that the proposed parameterization (28) may be valid. For the case studied, the mean values of the coefficients A and B are -3.63 and 6.57 respectively. There is also strong evidence that coefficients A and B are linearly related supporting the idea that these coefficients describe specific microphysical processes. However, our findings are still preliminary and should also be tested against cloud models.

5. SUMMARY AND CONCLUSIONS

A method for retrieving ice cloud optical and microphysical property profiles from millimeter cloud radar and lidar backscatter observations is introduced. The lidar-radar models introduced here target the complex nature of cirrus clouds; therefore, non-spherical effects due to ice crystals in cirrus clouds are parameterized through the use of area-, volume- and mass-diameter empirical relationships. Moreover, lidar model estimates multiple scatter contribution, while radar model accounts for Mie effects. The retrieval of cirrus cloud optical and microphysical properties follows a scheme that is framed around the optimal estimation method.

Analysis of the lidar-radar model mathematical formulation along with results obtained from its direct application to real aircraft data collected during the CRYSTAL-FACE experiment, demonstrated the following:

(i) The initial analysis of sensitivities and errors of the lidar-radar system indicates that IWC and D_0 are most reliably retrieved, whereas N_0 is the least reliable information derived from the retrievals.

(ii) The application of the lidar-radar model to measured data collected during CRYSTAL-FACE experiment, underlines once more the need of better knowledge about model parameters, with a special interest in the fit coef-

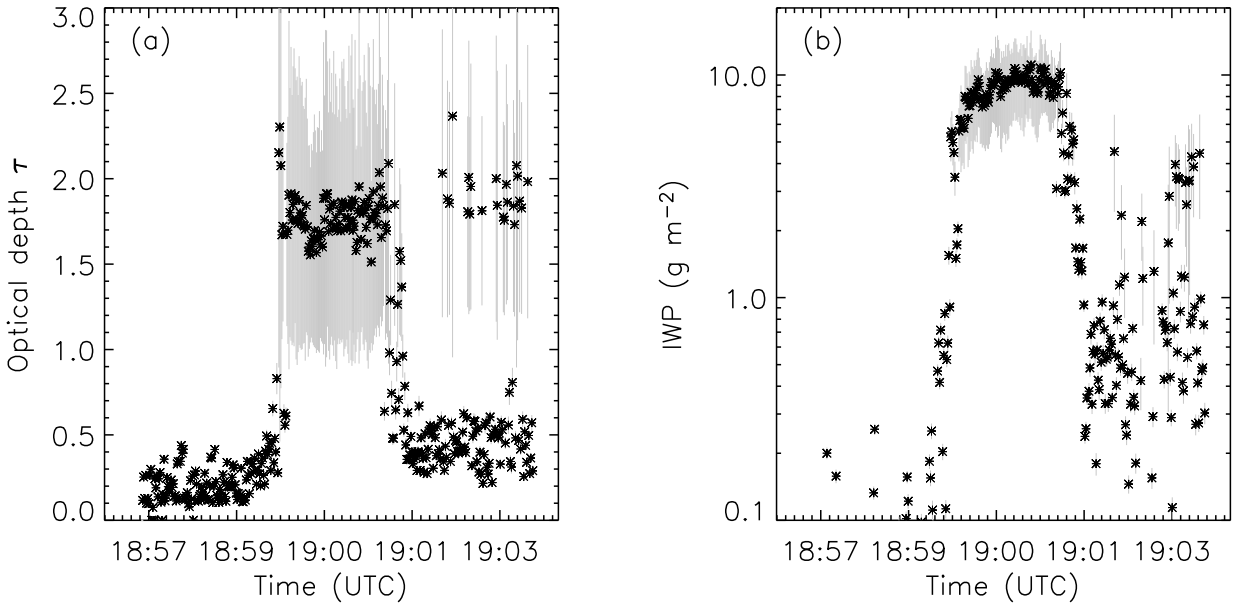

Figure 7: Calculated (a) Optical depth τ, and (b) IWP. Associated errors are with gray lines.

ficients describing the non-spherical effects of ice crystal particles.

(iii) Vertical profiles of N_0, D_0, and IWC deduced using CRYSTAL-FACE data show a complex, layered structure of the cirrus cloud microphysics. Comparison against measured data pointed out that the lidar-radar system is inefficient in detecting small ice crystals, but can reliably retrieve cloud averaged microphysical parameters.

(iv) The investigation of empirical relationships between various cloud parameters indicates that a distinct and robust relationship between N_0 and D_0 exists, that might offer insight into the nature of the microphysical processes taking place in cirrus. The $IWC - Z$ relationship derived in this particular case, further confirms similar previously reported behavior, thus validating the method.

The lidar-radar observing system described in this paper holds particular relevance to the Earth Observing System (EOS) CloudSat (Stephens et al., 2002) and Cloud-Aerosol Lidar and Infrared Pathfinder Satellite Observations satellite missions (www-calipso.larc.nasa.gov), scheduled for launch in Spring 2005.

6. ACKNOWLEDGMENTS

This research was funded by NASA Research Grant # NAG5-11475, while the first author was a a postdoctoral fellow at Colorado State University, Department of Atmospheric Science. We also gratefully acknowledge the support of our research sponsor, the Office of Naval Research under program element PE-0602435N. The authors are thankful to Drs. M. McGill, G. Heymsfield, L. Li, and Mr. D. Hlavka of Goddard Space Flight Center for providing radar and lidar data. Dr. E. Weinstock of Harvard University provided TWI data, while Dr.R. Lawson of SPEC Inc. provided SPP data.

7. REFERENCES

[1] Bohren, C. F. and D. R. Huffman, 1983: Absorption and Scattering of Light by Small Particles, *John Wiley & Sons*, (1983) 530 pp

[2] Brown, P. R. A., A. J. Illingworth, A. J. Heymsfield, G. M. McFarquhar, K. A. Browning and M. Gosset, 1995: The Role of Spaceborne Millimeter-Wave Radar in the Global Monitoring of Ice Cloud, *J. Applied Meteor.,* **34**, 2346-2366

[3] Brown, P. R. A. and P. N. Francis, 1995: Improved Measurements of the Ice Water Content in Cirrus using a Total-Water Probe, *J. Atmos. Oceanic Tech.,* **12**, 410-414

[4] Donovan, D. P. and A. C. A. P. van Lammeren, 2001: Cloud Effective Particle Size and Water Content Profile Retrievals Using Combined Lidar and Radar Observations 1. Theory and examples, *J. Geophys. Res.,* **106***,* 27425-27448

[5] Eloranta, E. W., 1998: Practical Model for the Calculation of Multiply Scattered Lidar Returns, *Appl. Optics,* **37**, 2464-2472

[6] Held, I. M. and B. J. Soden, 2000: Water vapor feedback and global warming, *Annu. Rev. Energy Environ.,* **25***,* 441-475

[7] Heymsfield, A. J. et al., 2004a: Effective Ice Particle Densities Derived from Aircraft Data, *J. Atmos. Sci.,* **61***,* 982-1003

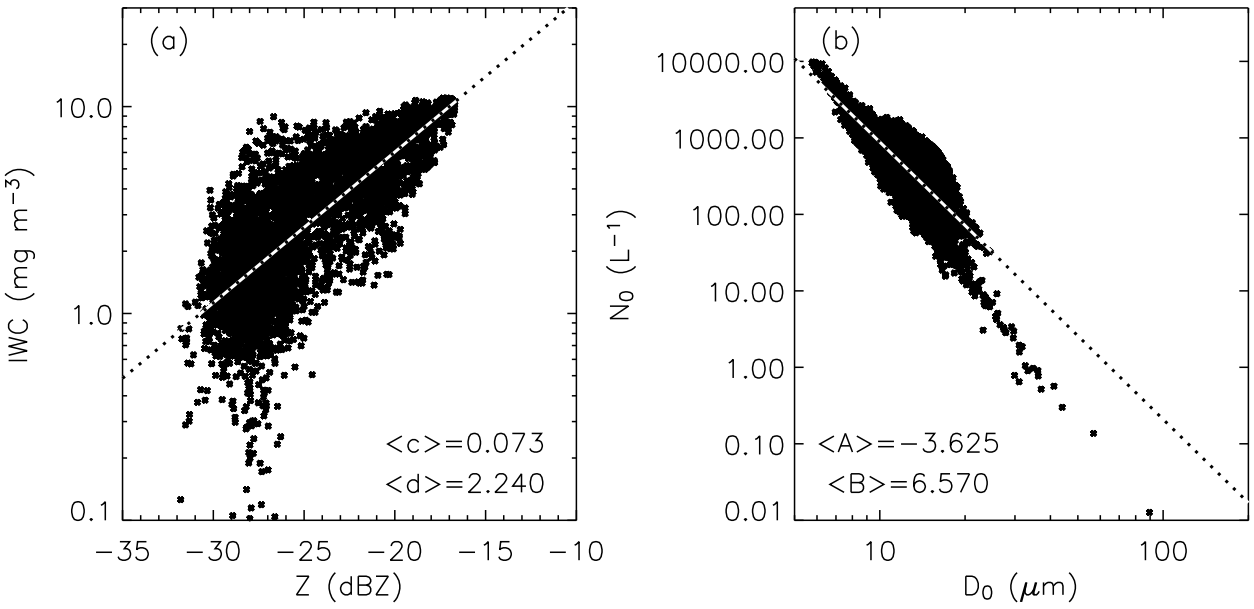

Figure 8: Scatter plots: (a) IWC vs. Z; (b) N_0 vs. D_0. Mean values and analytical fits (dotted lines) are also represented. See text for details.

[8] Heymsfield, A. J. et al., 2004b: Effective Ice Particle Densities for Cold Anvil Cirrus, *Geophys. Res. Lett.,* **31***,* L02101, doi:10.1029/2003GL018311

[9] Heymsfield, A. J. et al., 2002: Observations and Parameterizations of Particle Size Distributions in Deep Tropical Cirrus and Stratiform Precipitating Clouds: Results from In Situ Observations in TRMM Field Campaigns, *J. Atmos. Sci.,* **59***,* 3457-3491

[10] Heymsfield, A. J., 1972: Ice Crystals Terminal Velocities, *J. Atmos. Sci.,* **29***,* 1348-1357

[11] Jazwinsky, A. H., 1970: *Stochastic Processes and Filtering Theory*. Academic Press, 376 pp.

[12] Li, L., G. M. Heymsfield, P. E. Racette, L. Tian, and E. Zenker, 2004: The 94 GHz Cloud Radar System on a NASA ER-2 Aircraft, *J. Atmos. and Oceanic Tech.,* in review

[13] Liou, K. N., 1986: Influence of Cirrus Clouds on Weather and Climate Processes: A Global Perspective, *Mon. Wea. Rev.,* **114***,* 1167-1199

[14] McGill, M. J., D. L. Hlavka, W. D. Hart, E. J. Welton, and J. R. Campbell, 2003: Airborne Lidar Measurements of Aerosol Optical Properties During SAFARI-2000, *J. Geophys. Res.,* **108***,* doi:10.1029/2002JD002370

[15] Mitchell, D. L., A. Macke, and Y. Liu, 1996: Modeling Cirrus Clouds. Part II: Treatment of Radiative Properties, *J. Atmos. Sci.,* **53***,* 2967-2996

[16] Mitrescu, C., J. M. Haynes, G. L. Stephens, S. D. Miller et al., 2004: Cirrus Cloud Optical, Microphysical and Radiative Properties Observed During CRYSTAL-FACE Experiment: I. A Lidar-Radar Retrieval System, *J. Geophys. Res.,* in review

[17] Mitrescu, C., 2004: Lidar Model with Parameterized Multiple Scattering for Retrieving Cloud Optical Properties, accepted to *J. Quant. Spectrosc. Radiat. Transfer*

[18] Stephens, G. L. et al., 2002: The CloudSat Mission and the A-Train: A New Dimension of Space-Based Observations of Clouds and Precipitation, *Bull. Amer. Meteorol. Soc.,* **12** 1771-1790

[19] Stephens, G. L., R. J. Engelen, M. Vaughan, and T. L. Anderson, 2001: Toward Retrieving Properties of the Tenuous Atmosphere Using Space-Based Lidar Measurements, *J. Geophys. Res.,* **106***,* 28,143-28,157

[20] Verlinde, J., P. J. Flatau, and W. R. Cotton, 1990: Analytical Solutions to the Collection Growth Equation: Comparison with Approximate Methods and Application to Cloud Microphysics Parameterization Schemes, *J. Atmos. Sci.,* **47***,* 2871-2880

[21] Weinstock, E. M., et al., 1994: New Fast Response Photofragment Fluorescent Hygrometer for Use on the NASA ER-2 and the Perseus Remotely Piloted Aircraft, *Rev. Sci. Instrum.,* **65***,* 3544-3554